Astron. Astrophys. 354, 349–364 (2000)

ASTRONOMY AND ASTROPHYSICS

The structure of radiative shock waves

II. The multilevel hydrogen atom

Yu.A. Fadeyev[1] **and D. Gillet**[2]

[1] Institute for Astronomy of the Russian Academy of Sciences, Pyatnitskaya 48, 109017 Moscow, Russia (fadeyev@inasan.rssi.ru)
[2] Observatoire de Haute-Provence – CNRS, 04870 Saint-Michel l'Observatoire, France (gillet@obs-hp.fr)

Received 2 September 1999 / Accepted 16 November 1999

Abstract. Models of steady–state plane–parallel shock waves propagating through the unperturbed hydrogen gas of temperature $T_1 = 6000$K and density $\rho_1 = 10^{-10}$ gm cm^{-3} are computed for upstream velocities $15 \text{ km s}^{-1} \leq U_1 \leq 70 \text{ km s}^{-1}$. The properties of the ambient gas are typical for atmospheres of pulsating stars. The shock wave structure is considered in terms of the self–consistent solution of the radiation transfer, fluid dynamics and rate equations for $2 \leq L \leq 4$ atomic bound levels with a continuum. The radiative flux $F_{\rm R}$ emergent from the shock wave was found to be independent of the lower limit ν_L of the frequency range provided that $\nu_L < \nu_2$, where ν_2 is the Balmer continuum head frequency. At the same time the decrease of ν_L is accompanied by decrease of the Lyman continuum flux and leads to smaller heating and weaker ionization of the hydrogen gas in the radiative precursor. For all models the size of the radiative precursor is of $\sim 10^4$ cm and corresponds to several mean free paths of photons at the frequency of the Lyman continuum edge ν_1. The compression ratio at the discontinuous jump gradually increases with increasing upstream velocity U_1, reaches the maximum of $\rho^+/\rho^- = 3.62$ at $U_1 \approx 55 \text{ km s}^{-1}$ and slowly decreases for larger U_1 due to the strong rize of the preshock gas temperature. The radiative flux from the shock wave was determined as a function of the upstream velocity U_1 and its ratio to the total energy flux in the shock wave $\mathcal{C}_2$ was found to range within $0.18 < F_{\rm R}/\mathcal{C}_2 < 0.92$ for $15 \text{ km s}^{-1} \leq U_1 \leq 65 \text{ km s}^{-1}$. Thus, at upstream velocities $U_1 > 60 \text{ km s}^{-1}$ the shock wave losses more than 90% of its total energy due to radiation. For all shock wave models the role of collisional processes in both bound–bound and bound–free atomic transitions was found to be negligible in comparison with corresponding radiative processes.

Key words: shock waves – hydrodynamics – radiative transfer

1. Introduction

Attempts to obtain the self–consistent solution of the equations of fluid dynamics and radiative transfer for shock waves propagating through atmospheric gases were undertaken during several last decades. The need to employ the self–consistent solution is of tremendous importance in the case of the partially ionized preshock hydrogen gas undergoing the substantial radiative heating and photoionization due to the strong absorption of the Lyman continuum radiation outgoing from the postshock region. In order to correctly treat the coupling between the preshock and postshock regions the two different methods known as the "mean–photon approximation" and the "asymptotic layering method" were previously proposed (see, for recent review, Gillet 1999). Unfortunately, in both these methods the radiative transfer is treated as an initial value problem which is solved with use of the shooting method. The principal disadvantage of such an approach is that the true solution of the transfer equation is unstable for optical depths $\tau > 1$ since it is affected by the exponentially growing errors. This obstacle, however, can be overcome if the radiative transfer is solved as a two–point boundary value problem. In order to reach the self–consistency between the gas flow and the radiation field Fadeyev & Gillet (1998, hereinafter referred to as Paper I) employed the procedure of global iterations. Each cycle of the global iteration procedure involves the solution of the initial–value problem for the fluid dynamics and rate equations which is followed by the solution of the two–point boundary value problem for the radiation transfer equation. As was shown in Paper I, the global iterations converge and provide with the stable self–consistent solution.

The goal of this study has been to further develop a method of global iterations for calculating the structure of radiative shock waves. In Paper I the study was restricted to the model of the hydrogen atom with two bound levels and a continuum. The rate equations were solved for the first bound level and free electrons, whereas the second atomic level was treated in LTE. In our previous study we did not take into account also the rise of the electron temperature due to the adiabatic compression at the discontinuous jump. Moreover, the convergence of global iterations has been reached for shock models with insufficiently thick postshock region. As a result, the models presented in Paper I did not cover the full recombination of the hydrogen and estimates of the total radiative flux emergent from the shock wave remained uncertain.

In the present work the system of the ordinary differential equations is extended by the terms taking into account the con-

tribution of the radiation field in the energy and momentum equations. The rate equations are solved for all bound levels of the adopted hydrogen atom model. The substantial improvements of the computer program allowed us to obtain the good convergence of global iterations for shock wave models involving almost the entire recombination zone and, thereby, to obtain the reliable estimates of the radiative flux emergent from shock waves with upstream Mach numbers as large as $M_1 \approx 7$. As in Paper I, the present study is confined to shock waves propagating through the partially ionized hydrogen gas.

The present paper is organized as follows. In Sect. 2 we describe details of our shock wave model, give the fluid dynamics and rate equations written in the form of the ordinary differential equations and describe the solution of the transfer equation for the both continuum and spectral line radiation. In comparison with Paper I the equations are completely rewritten with the use of more convenient notations and should replace those of Paper I where numerous typographical errors resulted from the missing of the TEX macro definition file. In Sect. 3 we discuss the properties of the solution, demonstrate its convergence and degree of approximation. General properties of the shock wave models are presented in Sect. 4. More detailed description of the models is given in Sects. 5 – 7 where we discuss the properties of the radiation field and the structure of the preshock and postshock regions, respectively.

2. Basic equations

We consider steady–state, plane–parallel shock waves propagating through the homogeneous medium composed solely of an atomic hydrogen gas. The solution is determined as a function of three parameters: the unperturbed gas temperature T_1, the unperturbed gas density ρ_1 and the velocity U_1 at which the shock wave moves with respect to the ambient gas. The model is represented by a flat finite slab comoving with the shock wave and the origin is set at the infinitesimally thin discontinuous jump (adiabatic shock front) where thermodynamic quantities undergo an abrupt change.

As was shown in Paper I, the stable self–consistent solution for the radiative shock wave structure can be obtained with the method of global iterations. In this method the rate equations for atomic level populations and equations of fluid dynamics are treated as an initial–value problem for the system of ordinary differential equations, whereas the radiation transfer is solved in the framework of the two–point boundary value problem. The interplay between the gas flow and the radiation field is taken into account by the iteration procedure. Such an approach allows us to substantially diminish the role of the stiffness of the rate equations as well as to avoid large errors arising due to the strong frequency dependence of the radiation field.

In order to apply the Feautrier technique (Feautrier 1964) for solution of the transfer equation the slab is divided into $N-1$ cells (see, e.g., Mihalas 1978). The cell sizes increase in both directions from the discontinuous jump locating at the $\mathcal{J}$–th cell interface with space coordinate $X_{\mathcal{J}} = 0$. In cell interfaces with space coordinates X_j, where $1 \le j \le N$, we define the monochromatic optical depth $\tau_{\nu j}$ and the monochromatic radiative flux $F_{\nu j}$ at frequency ν. Other variables are defined at the cell centers with space coordinates

$$X_{j-1/2} = \frac{1}{2}\left(X_{j-1} + X_j\right), \qquad (j = 2, \ldots, N). \tag{1}$$

The outer boundaries of the preshock and postshock regions are X_1 and X_N, respectively. For these boundary points we write

$$X_{1/2} = X_1, \qquad X_{N+1/2} = X_N \tag{2}$$

since all variables must be also defined at both boundaries.

Integration of the ordinary differential equations begins at the preshock outer boundary X_1 where the gas is assumed to be unperturbed and the number densities of free electrons $n_{\rm e}$ and bound atomic levels n_i are in statistical equilibrium with radiation field of the shock wave. Preshock integration is done on the interval $[X_1, X_{\mathcal{J}-1/2}]$, where $X_{\mathcal{J}-1/2}$ is the space coordinate of the cell center just ahead the discontinuous jump. Initial conditions for the postshock integration are obtained from the Rankine–Hugoniot equations relating variables at the cell centers $X_{\mathcal{J}-1/2}$ and $X_{\mathcal{J}+1/2}$. The outer boundary of the postshock region X_N is set behind the recombination zone. When integration of the ordinary differential equations on the interval $[X_{\mathcal{J}+1/2}, X_N]$ is completed, we solve the transfer equation for the whole slab. Below we discuss the steps of the global iteration procedure in more detail.

2.1. Rankine–Hugoniot relations

The zonal quantities at the cell centers $X_{\mathcal{J}-1/2}$ and $X_{\mathcal{J}+1/2}$ are related by the radiation modified Rankine–Hugoniot equations (Marshak 1958)

$$\rho U = \mathcal{C}_0 \equiv \dot{m}, \tag{3}$$

$$\dot{m}U + P_{\rm g} + P_{\rm R} = \mathcal{C}_1, \tag{4}$$

$$\dot{m}\left(h + \frac{1}{2}U^2\right) + F_{\rm R} + U\left(E_{\rm R} + P_{\rm R}\right) = \mathcal{C}_2, \tag{5}$$

where $E_{\rm R}$, $F_{\rm R}$ and $P_{\rm R}$ are the radiation energy density, radiation flux and radiation pressure, respectively,

$$P_{\rm g} = P_a + P_{\rm e} = n_{\rm H} k T_a + n_{\rm e} k T_{\rm e} \tag{6}$$

is the gas pressure, $n_{\rm H}$ and T_a are the number density and the temperature of hydrogen atoms both neutral and ionized, $T_{\rm e}$ is the temperature of free electrons. The specific enthalpy is

$$h = \frac{5}{2}\frac{n_{\rm H}}{\rho} k T_a + \frac{5}{2}\frac{n_{\rm e}}{\rho} k T_{\rm e} + \frac{E_{\rm ex}}{\rho} + \frac{E_{\rm I}}{\rho}, \tag{7}$$

where

$$E_{\rm ex} = \chi_{\rm H} \sum_{i=1}^{L} \left(1 - i^{-2}\right) n_i \tag{8}$$

is the excitation energy, L is the number of bound atomic levels, $E_{\rm I} = \chi_{\rm H} n_{\rm e}$ is the ionization energy, $\chi_{\rm H}$ is the ionization potential of the hydrogen atom.

Eqs. (3) – (5) are solved for the compression ratio

$$\eta = \frac{\rho^+}{\rho^-} = \frac{U^-}{U^+}, \tag{9}$$

where superscripts minus and plus denote for brevity the quantities defined at cell centers $X_{\jmath-1/2}$ and $X_{\jmath+1/2}$, respectively.

Substituting (6) and (7) into (4) and (5) and then combining two resulting equations we obtain

$$A\eta^2 - B\eta + C = 0, \tag{10}$$

where

$$A = \left(a_{\rm T}^-\right)^2 + \frac{\left(U^-\right)^2}{5} + \frac{2}{5}\frac{F_{\rm R}^- - F_{\rm R}^+}{\dot{m}} + \frac{2}{5}\frac{E_{\rm R}^- + P_{\rm R}^-}{\rho^-}, \tag{11}$$

$$B = \left(a_{\rm T}^-\right)^2 + \left(U^-\right)^2 + \frac{P_{\rm R}^- - P_{\rm R}^+}{\rho^-} - \frac{2}{5}\frac{E_{\rm R}^+ + P_{\rm R}^+}{\rho^-}, \tag{12}$$

$$C = \frac{4}{5}\left(U^-\right)^2, \tag{13}$$

and $a_{\rm T} = (P_{\rm g}/\rho)^{1/2}$ is the isothermal sound speed.

The postshock electron temperature $T_{\rm e}^+$ is determined in the assumption of the adiabatic compression of the electron gas:

$$T_{\rm e}^+ = \eta^{\gamma-1} T_{\rm e}^-, \tag{14}$$

where $\gamma = \frac{5}{3}$ is the ratio of specific heats. The postshock temperature of heavy particles is

$$\begin{aligned} T_a^+ \;=\; & T_a^- + \frac{n_{\rm e}^-}{n_{\rm H}^-}\left(T_{\rm e}^- - T_{\rm e}^+\right) + \frac{1}{5}\frac{\dot{m}U^-}{n_{\rm H}^- k}\left(1 - \frac{1}{\eta^2}\right) + \\ & + \frac{2}{5}\frac{F_{\rm R}^- - F_{\rm R}^+}{n_{\rm H}^- k U^-} + \frac{2}{5}\frac{E_{\rm R}^- - P_{\rm R}^- - E_{\rm R}^+ - P_{\rm R}^+}{n_{\rm H}^- k}. \end{aligned} \tag{15}$$

The last two terms in (11), (12) and (15) take into account the contribution of the radiation field which rapidly increases with increasing upstream velocity. However, for models considered in the present study this contribution was found to be rather small. For example, at the upstream velocity of $U_1 = 70\,{\rm km\,s^{-1}}$ omitting of these terms leads to the increase of the compression ratio η by nearly one percent and to the increase of the postshock temperature T_a^+ by less than one tenth of the percent. Nevertheless, we retain these terms in Eqs. (4) and (5) in order to use the momentum flux $\mathcal{C}_1$ and the total energy flux $\mathcal{C}_2$ for checking the accuracy of the model throughout the slab.

2.2. Fluid dynamics and rate equations

The solution vector of the system of ordinary differential equations is

$$\mathbf{Y} = \{\tilde{n}_1, \ldots, \tilde{n}_L, \tilde{n}_{\rm e}, \widetilde{E}_a, \widetilde{E}_{\rm e}, U\}, \tag{16}$$

where $E_a = \frac{3}{2} n_{\rm H} k T_a$ and $E_{\rm e} = \frac{3}{2} n_{\rm e} k T_{\rm e}$ are the translational energies of hydrogen atoms and free electrons per unit volume, respectively. Here and below the tilde denotes the quantities expressed per unit mass, that is, $\tilde{n}_i = n_i/\rho$, $\widetilde{E}_a = E_a/\rho$ etc.

The assumption of the one–dimensional steady flow in planar geometry implies that throughout the slab the continuity equation is written as $\rho U = \dot{m} \equiv \mathcal{C}_0$. Thus, the system of the fluid dynamics and rate equations is

$$\frac{d\tilde{n}_i}{dt} \;=\; \sum_{\substack{j=1\\ j\neq i}}^{L} \tilde{n}_j P_{ji} + \tilde{n}_{\rm e} P_{\kappa i} - \tilde{n}_i \sum_{\substack{j=1\\ j\neq i}}^{L} P_{ij} - \tilde{n}_i P_{i\kappa}, \tag{17}$$

$$\frac{d\tilde{n}_{\rm e}}{dt} \;=\; \sum_{i=1}^{L} \tilde{n}_i P_{i\kappa} - \tilde{n}_{\rm e} \sum_{i=1}^{L} P_{\kappa i}, \tag{18}$$

$$\frac{d\widetilde{E}_a}{dt} \;=\; -P_a \frac{dV}{dt} - Q_{\rm elc}, \tag{19}$$

$$\frac{d\widetilde{E}_{\rm e}}{dt} \;=\; -P_{\rm e} \frac{dV}{dt} + Q_{\rm elc} + Q_{\rm inc} - \frac{1}{\rho}\frac{dE_{\rm R}}{dt}, \tag{20}$$

$$\frac{dU}{dt} \;=\; -\frac{1}{\dot{m}}\frac{dP_{\rm g}}{dt} + \frac{1}{\rho c}\int_0^\infty \chi_\nu F_\nu \, d\nu, \tag{21}$$

where P_{ij} and P_{ji} are the total (collisional plus radiative) rates of bound–bound upward and downward transitions between the i–th and j–th atomic levels, respectively, $P_{i\kappa}$ and $P_{\kappa i}$ are the total rates of ionizations and recombinations for the i–th atomic level, $Q_{\rm elc}$ and $Q_{\rm inc}$ are the rates of energy gain by electron gas in elastic and inelastic collisions, respectively, χ_ν is the monochromatic extinction coefficient, $V = 1/\rho$ is the specific volume, c is the velocity of light.

Eqs. (17) – (21) are written for time derivatives in their left–hand–sides, whereas for calculation of the shock wave spatial structure it is more convenient to integrate the differential equations with respect to the space coordinate X. Furthermore, the time derivatives of the gas pressure and specific volume should be expressed in terms of integrated variables. Differentiating (6) and (4) we have

$$\frac{dP_{\rm g}}{dt} = \frac{2}{3}\rho\left(\frac{d\widetilde{E}_a}{dt} + \frac{d\widetilde{E}_{\rm e}}{dt}\right) - \rho P_{\rm g}\frac{dV}{dt}. \tag{22}$$

and

$$\frac{dV}{dt} = -\frac{1}{\dot{m}^2}\left(\frac{dP_{\rm g}}{dt} + \frac{dP_{\rm R}}{dt}\right). \tag{23}$$

Substituting (22) and

$$\frac{dP_{\rm R}}{dt} = -\frac{U}{c}\int_0^\infty \chi_\nu F_\nu \, d\nu. \tag{24}$$

into (23) we write the time derivative of the specific volume as

$$\frac{dV}{dt} = -\mathcal{A}\left(\frac{d\widetilde{E}_a}{dt} + \frac{d\widetilde{E}_{\rm e}}{dt}\right) + \mathcal{F}, \tag{25}$$

where

$$\mathcal{A} = \left[\frac{3}{2}\dot{m}U\left(1 - \beta^2\right)\right]^{-1}, \tag{26}$$

$$\mathcal{F} = \frac{1}{\dot{m}\,(1-\beta^2)\,\rho c}\int\limits_0^\infty \chi_\nu F_\nu d\nu, \tag{27}$$

and $\beta = a_{\rm T}/U$.

With (22) and (25) Eqs. (17) – (21) can be rewritten as

$$U\frac{d\tilde{n}_i}{dX} = \sum_{\substack{j=1\\ j\neq i}}^{L}\tilde{n}_j P_{ji} + \tilde{n}_{\rm e}P_{\kappa i} - \tilde{n}_i\sum_{\substack{j=1\\ j\neq i}}^{L}P_{ij} - \tilde{n}_i P_{i\kappa}, \tag{28}$$

$$U\frac{d\tilde{n}_{\rm e}}{dX} = \sum_{i=1}^{L}\tilde{n}_i P_{i\kappa} - \tilde{n}_{\rm e}\sum_{i=1}^{L}P_{\kappa i}, \tag{29}$$

$$U\frac{d\widetilde{E}_a}{dX} = \frac{\mathcal{A}P_a}{1-\mathcal{A}P_{\rm g}}Q_{\rm inc} - Q_{\rm elc} - U\mathfrak{R}_a, \tag{30}$$

$$U\frac{d\widetilde{E}_{\rm e}}{dX} = \frac{1-\mathcal{A}P_a}{1-\mathcal{A}P_{\rm g}}Q_{\rm inc} + Q_{\rm elc} - U\mathfrak{R}_{\rm e}, \tag{31}$$

$$\frac{dU}{dX} = -\mathcal{A}\dot{m}\frac{d\widetilde{E}_a}{dX} - \mathcal{A}\dot{m}\frac{d\widetilde{E}_{\rm e}}{dX} + \mathfrak{R}_{\rm U}, \tag{32}$$

where the terms

$$\mathfrak{R}_a = \left(\frac{1-\mathcal{A}P_{\rm e}}{1-\mathcal{A}P_{\rm g}}P_a + \frac{\mathcal{A}P_a}{1-\mathcal{A}P_{\rm g}}P_{\rm e}\right)\frac{\mathcal{F}}{U} + \\ + \frac{\mathcal{A}P_a}{1-\mathcal{A}P_{\rm g}}\frac{1}{\dot{m}}\frac{dE_{\rm R}}{dt}, \tag{33}$$

$$\mathfrak{R}_{\rm e} = \left(\frac{\mathcal{A}P_{\rm e}}{1-\mathcal{A}P_{\rm g}}P_a + \frac{1-\mathcal{A}P_a}{1-\mathcal{A}P_{\rm g}}P_{\rm e}\right)\frac{\mathcal{F}}{U} + \\ + \frac{1-\mathcal{A}P_a}{1-\mathcal{A}P_{\rm g}}\frac{1}{\dot{m}}\frac{dE_{\rm R}}{dt}, \tag{34}$$

and

$$\mathfrak{R}_{\rm U} = \rho\mathcal{F} \tag{35}$$

take into account the contribution of the radiation field and can be omitted if $E_{\rm R} \ll E_a + E_{\rm e}$ and $P_{\rm R} \ll P_{\rm g}$.

The excitation rate per atom in the i–th initial state is

$$P_{ij} = n_{\rm e}C_{ij} + R_{ij} \tag{36}$$

and the de–excitation rate per atom in the j–th initial states is

$$P_{ji} = \frac{n_i^*}{n_j^*}\left(n_{\rm e}C_{ij} + R_{ij}^\dagger\right), \tag{37}$$

where n_i^* and n_j^* are the bound–level number densities of hydrogen atoms in i–th and j–th state given by the Saha–Boltzmann equation for the actual non–equilibrium number density of free electrons $n_{\rm e}$.

The collisional excitation rate is

$$C_{ij} = \frac{h^2}{(2\pi m_{\rm e})^{3/2}k^{1/2}}\frac{\sum\limits_{ll'}\Gamma_{iljl'}}{g_j T_{\rm e}^{1/2}}\exp\left(\frac{\chi_{\rm H}}{i^2} - \frac{\chi_{\rm H}}{j^2}\right), \tag{38}$$

where g_j is the statistical weight of level j and $\Gamma_{iljl'}$ is the effective collision strength. In the present study the effective collision strengths were evaluated from analytic fits by Scholz & Walters (1991) for $1s-2$ transitions, Callaway & Unnikrishnan (1993) for $1s-3$ transitions and Callaway (1994) for $2-3$ transitions. For other transitions the effective collision strengths were calculated using the Chebyshev polynomial fits of the data by Aggarwal et al. (1991).

The photoexcitation rates are given by

$$R_{ij} = 4\pi\int\limits_0^\infty \frac{\alpha_{ij}(\nu)}{h\nu}J_\nu d\nu, \tag{39}$$

where $\alpha_{ij}(\nu)$ is the spectral line absorption cross–section in transition $i \to j$ and J_ν is the monochromatic mean intensity. The rate of downward (spontaneous plus induced) radiative transitions $j \to i$ is

$$\frac{n_i^*}{n_j^*}R_{ij}^\dagger = \frac{n_i^*}{n_j^*}4\pi\int\limits_0^\infty \frac{\alpha_{ij}(\nu)}{h\nu}\left(\frac{2h\nu^3}{c^2} + J_\nu\right)\exp\left(-\frac{h\nu}{kT_{\rm e}}\right). \tag{40}$$

The total rate of ionizations from the i–th level is

$$P_{i\kappa} = n_{\rm e}C_{i\kappa} + R_{i\kappa} \tag{41}$$

and the total rate of recombinations to the i–th level is

$$P_{\kappa i} = \frac{n_i^*}{n_\kappa^*}\left(n_{\rm e}C_{i\kappa} + R_{i\kappa}^\dagger\right), \tag{42}$$

where n_κ^* is the number density of hydrogen ions evaluated from the Saha–Boltzmann equation for the actual non–equilibrium number density of free electrons $n_{\rm e}$. The collisional ionization rate is

$$C_{i\kappa} = n_{\rm e}\pi a_0^2\left(\frac{8k}{m_{\rm e}\pi}\right)^{1/2}T_{\rm e}^{1/2}\exp\left(-\frac{\chi_i}{kT_{\rm e}}\right)\Gamma_i(T_{\rm e}), \tag{43}$$

where χ_i is the potential of ionization from the i–th level, the $\Gamma(T_{\rm e})$ is a slowly–varying function of $T_{\rm e}$ evaluated with fitting formulae given by Mihalas (1967). The rates of photoionizations and photorecombinations are

$$R_{i\kappa} = 4\pi\int\limits_0^\infty \frac{\alpha_{\rm bf}(i,\nu)}{h\nu}J_\nu d\nu \tag{44}$$

and

$$\frac{n_i^*}{n_\kappa^*}R_{i\kappa}^\dagger = \frac{n_i^*}{n_\kappa^*}4\pi\int\limits_0^\infty \frac{\alpha_{\rm bf}(i,\nu)}{h\nu}\left(\frac{2h\nu^3}{c^2} + J_\nu\right)e^{-h\nu/kT_{\rm e}}d\nu, \tag{45}$$

where $\alpha_{\rm bf}(i,\nu)$ is the bound–free absorption cross section at frequency ν by hydrogen atoms in the i–th state. As is shown below, the role of collisional processes in the both bound–bound and bound–free transitions throughout the radiative shock wave is negligible since their rates are smaller by several orders of magnitude in comparison with rates of radiative transitions.

The rate of energy gain by electrons in inelastic collisions is (Murty 1971)

$$Q_{\rm inc} = -\frac{d\widetilde{E}_{\rm I}}{dt} - \frac{d\widetilde{E}_{\rm ex}}{dt} - \frac{1}{\rho}\nabla\cdot\mathbf{F}_{\rm R}, \tag{46}$$

where

$$\nabla \cdot \mathbf{F}_{\rm R} = 4\pi \int\limits_0^\infty (\eta_\nu - \kappa_\nu J_\nu)\, d\nu \tag{47}$$

is the divergence of radiative flux, η_ν and κ_ν are the emission and absorption coefficients, respectively.

Behind the discontinuous jump the temperature of heavy particles T_a exceeds the electron temperature $T_{\rm e}$ and free electrons acquire the energy in elastic collisions with heavy particles. The rate of energy gain in elastic collisions is a sum of the rates corresponding to collisions with hydrogen ions and neutral hydrogen atoms:

$$Q_{\rm elc} = Q_{\rm ei} + Q_{ea}. \tag{48}$$

The rate of energy gain in elastic collisions with hydrogen ions is (Spitzer & Härm 1953)

$$Q_{\rm ei} = \frac{2}{3}\frac{n_{\rm e}}{\rho} k \frac{T_a - T_{\rm e}}{t_{\rm eq}}\,, \tag{49}$$

where

$$t_{\rm eq} = \frac{252 T_{\rm e}^{3/2}}{n_{\rm e} \ln\Lambda} \tag{50}$$

is the equipartition time and

$$\Lambda = 9.43 + 1.15 \log\left(T_{\rm e}^3/n_{\rm e}\right). \tag{51}$$

The rate of energy gain by electrons in elastic collisions with neutral hydrogen atoms is

$$Q_{ea} = \frac{n_{\rm e}}{n_{\rm H}} \frac{m_{\rm e}}{m_{\rm H}} n_1 \frac{T_a - T_{\rm e}}{T_{\rm e}} \langle \sigma_{ea} v^3 \rangle, \tag{52}$$

where the elastic scattering cross section is (Narita 1973)

$$\langle \sigma_{ea} v^3 \rangle = \int\limits_0^\infty \sigma_{ea} v^3 f(v)\, dv =$$
$$= 4\pi a_0^2 \left(\frac{8}{\pi}\right) \left(\frac{kT_{\rm e}}{m_{\rm e}}\right)^{3/2} \left[4 + \frac{24}{\left(1 + 2\cdot 10^{-5} T_{\rm e}\right)^3}\right]. \tag{53}$$

2.3. Radiation transfer equation

The quasi–static radiation transfer equation for the planar geometry is

$$\mu \frac{dI_{\mu\nu}}{d\tau_\nu} = I_{\mu\nu} - S_\nu, \tag{54}$$

where $I_{\mu\nu}$ is the specific intensity of radiation at the directional cosine $\mu = \cos(\theta)$ at frequency ν, $S_\nu = \eta_\nu/\kappa_\nu$ is the monochromatic source function and τ_ν is the monochromatic optical depth defined as $d\tau_\nu = \chi_\nu dX$. The absorption and extinction coefficient are

$$\kappa_\nu = \kappa_{\rm bf}(\nu) + \kappa_{\rm ff}(\nu) + \kappa_\ell(\nu) \tag{55}$$

and

$$\chi_\nu = \kappa_\nu + n_1 \sigma_{\rm R}(\nu) + n_{\rm e}\sigma_{\rm T}\,, \tag{56}$$

where $\kappa_{\rm bf}(\nu)$ is the bound–free absorption coefficient, $\kappa_{\rm ff}(\nu)$ is the free–free absorption coefficient, $\sigma_{\rm R}(\nu)$ is the cross section of the Rayleigh scattering by hydrogen atoms in the ground state, $\sigma_{\rm T}$ is the Thomson scattering cross section, $\kappa_\ell(\nu)$ is the spectral line absorption coefficient. Expressions for $\kappa_{\rm bf}(\nu)$ and $\kappa_{\rm ff}(\nu)$ can be found, for example, in the book by Mihalas (1978). The Rayleigh scattering cross section $\sigma_{\rm R}(\nu)$ was evaluated using the fitting formulae given by Kurucz (1970).

The continuum emission coefficient is

$$\eta_\nu = \frac{2h\nu^3}{c^2} e^{-h\nu/kT_{\rm e}} \left[\sum_{i=1}^{L} n_i^* \alpha_{\rm bf}(i,\nu) + n_{\rm e}^2 \alpha_{\rm ff}(\nu, T_{\rm e})\right], \tag{57}$$

where

$$\alpha_{\rm ff}(\nu, T_{\rm e}) = \frac{4e^6}{3ch} \left(\frac{2\pi}{3km_{\rm e}^3}\right)^{1/2} \frac{g_{\rm ff}(\nu, T_{\rm e})}{\nu^3 \sqrt{T_{\rm e}}} \tag{58}$$

is the free–free absorption cross section and $g_{\rm ff}(\nu, T_{\rm e})$ is the free–free Gaunt factor.

The spectral line absorption and emission coefficients are computed in the assumption of the complete redistribution, that is,

$$\kappa_\ell(\nu) = \frac{n_i B_{ij} h\nu_{ij}}{4\pi} \left(1 - \frac{n_j g_i}{n_i g_j}\right) \phi_\nu \tag{59}$$

and

$$\eta_\ell(\nu) = \frac{h\nu_{ij}}{4\pi} A_{ji} n_j \phi_\nu, \tag{60}$$

where g_i and g_j are statistical weights, A_{ji} and B_{ij} are Einstein coefficients, ϕ_ν is the spectral line absorption profile. Thus, we take into account the frequency dependence of the source function $S_\ell(\nu) = \eta_\ell(\nu)/\kappa_\ell(\nu)$ within the spectral line profile.

The radiative transfer problem is subject to the boundary conditions implying that the incident radiation on both faces of the slab is due to the thermal equilibrium radiation from the ambient unperturbed medium:

$$I^+_{\mu\nu 1/2} = I^-_{\mu\nu N+1/2} = B_\nu(T_1), \tag{61}$$

where $B_\nu(T_1)$ is the Planck function, T_1 is the temperature of the unperturbed gas and superscripts minus and plus correspond to $\mu < 0$ and $\mu > 0$, respectively. The transfer equation (54) with boundary conditions (61) is solved for the symmetric intensity average

$$u_{\mu\nu j-1/2} = \frac{1}{2}\left(I^+_{\mu\nu j-1/2} + I^-_{\mu\nu j-1/2}\right) \tag{62}$$

defined in the angle range $0 \le \mu \le 1$ (Feautrier 1964). The main difficulty arising in the solution of the transfer equation for the shock wave is due to the very small optical depth intervals $\Delta\tau_\nu$ in the vicinity of $X_\jmath = 0$ at frequencies lower than the ionization threshold of the level $i = 3$. In the present study this difficulty was overcome with use of the improved Feautrier

solution proposed by Rybicki & Hummer (1991) which provides the better numerical conditioning and prevents the lost of machine accuracy in the matrix elimination scheme.

In each cell center the intensity average $u_{\mu\nu j-1/2}$ is determined for sets of frequency and angle points. In order to compute the frequency integrals the continuum frequency range is divided into intervals with boundaries at the threshold ionization frequencies ν_i. The upper boundary of the continuum frequency range is ν_0. Continuum intervals are represented by $n_{\rm c}$ nodes of the Gauss–Legendre quadratures and spectral lines are represented by n_ℓ nodes. The radiation energy density $E_{\rm R}$, radiative flux $F_{\rm R}$ and radiation pressure $P_{\rm R}$ are determined by summation of frequency integrals over continuum intervals and over spectral lines:

$$E_{\rm R} = \sum_{i=1}^{L_{\rm c}} \frac{4\pi}{c} \int\limits_{\nu_i}^{\nu_{i-1}} J_\nu d\nu + \sum_{i=1}^{L_\ell} \frac{4\pi}{c} \int\limits_{\nu_i-\Delta\nu_i}^{\nu_i+\Delta\nu_i} J_\nu d\nu, \tag{63}$$

$$F_{\rm R} = \sum_{i=1}^{L_{\rm c}} 4\pi \int\limits_{\nu_i}^{\nu_{i-1}} H_\nu d\nu + \sum_{i=1}^{L_\ell} 4\pi \int\limits_{\nu_i-\Delta\nu_i}^{\nu_i+\Delta\nu_i} H_\nu d\nu, \tag{64}$$

$$P_{\rm R} = \sum_{i=1}^{L_{\rm c}} \frac{4\pi}{c} \int\limits_{\nu_i}^{\nu_{i-1}} K_\nu d\nu + \sum_{i=1}^{L_\ell} \frac{4\pi}{c} \int\limits_{\nu_i-\Delta\nu_i}^{\nu_i+\Delta\nu_i} K_\nu d\nu, \tag{65}$$

where $L_{\rm c}$ is the number of frequency intervals, L_ℓ is the number of spectral lines, $\Delta\nu_i$ is the half–width of the i–th spectral line frequency interval. The moments of the radiation field in Eddington's notation are

$$J_\nu = \int\limits_0^1 u_{\mu\nu} d\mu, \tag{66}$$

$$H_\nu = \int\limits_0^1 v_{\mu\nu} \mu d\mu, \tag{67}$$

$$K_\nu = \int\limits_0^1 u_{\mu\nu} \mu^2 d\mu, \tag{68}$$

where

$$v_{\mu\nu} = -\mu \frac{du_{\mu\nu}}{d\tau_\nu} = \frac{1}{2} \left(I^+_{\mu\nu} - I^-_{\mu\nu} \right) \tag{69}$$

is the antisymmetric flux–like average.

3. Properties of the solution

The thickness of the adiabatic compression region where thermodynamic variables undergo an abrupt change is only a few particle mean free paths. Therefore, in comparison with the whole shock wave the adiabatic compression region can be treated to a high degree of approximation as an infinitesimally thin discontinuous jump. The assumption of the steady–state flow allows us to represent the shock wave by the flat finite slab comoving with the discontinuous jump, so that the integration of the fluid dynamics and rate equations follows the element of gas which passes through the slab. The axis of the space coordinate X is chosen in such a way that the velocity of the gas element is $U = dX/dt > 0$ and the radiative flux emergent from the preshock and postshock outer boundaries is $F_1 < 0$ and $F_N > 0$, respectively.

For all models the space coordinate of the preshock outer boundary is $X_1 = -10^5$ cm, that is the size of the preshock region exceeds by an order of magnitude the size of the radiative precursor. The gas element crosses the preshock outer boundary at temperature T_1, density ρ_1 and velocity U_1. The radiative field at the preshock outer boundary is non–equilibrium, so that the number densities of hydrogen atoms in i–th state n_i and the number density of free electrons $n_{\rm e}$ should be evaluated from the solution of the equations of statistical equilibrium rather than in LTE approximation. To this end we solve Eqs. (17) and (18) with time derivatives equated to zero using the Newton–Raphson iteration procedure (see, e.g., Mihalas 1978). It should be noted, however, that the number densities obtained from the solution of the equations of statistical equilibrium do not differ substantially from their counterparts given by the Saha–Boltzmann equation. For example, the hydrogen ionization degree at the preshock outer boundary is in the range $8.9 \cdot 10^{-3} < x_{\rm H} < 2.5 \cdot 10^{-2}$ for upstream gas flow velocities $15 \ {\rm km \ s^{-1}} \le U_1 \le 70 \ {\rm km \ s^{-1}}$, whereas the LTE hydrogen ionization degree is $x_{\rm H} = 8.4 \cdot 10^{-3}$. Departure coefficients

$$b_i = \frac{n_i/n_i^*}{n_\kappa/n_\kappa^*} \tag{70}$$

of the first three levels change from $\mathbf{b} = \{0.9, 1.1, 1.1\}$ to $\mathbf{b} = \{0.1, 0.3, 0.9\}$ for the same range of U_1.

Of great importance is the choice of the space coordinate X_N of the postshock outer boundary. In particular, the slab should involve the layers of the full hydrogen recombination since otherwise the total radiative flux emergent from the shock is underestimated. Test calculations show that for the postshock outer boundary located behind the maximum of the hydrogen ionization the total radiative flux asymptotically approaches its limiting value with increasing X_N. At the same time, the increase of X_N is accompanied by the growth of the oscillation amplitude of iterated variables in the outermost layers of the postshock region, so that for too large X_N the global iterations ultimately diverge. This occurs mostly due to the limited accuracy of integration of the ordinary differential Eqs. (28) – (32). In the present study the space coordinate X_N was determined for each shock wave model from trial computations and ranged from $X_N = 5 \cdot 10^5$ cm for $U_1 = 70 \, {\rm km \, s^{-1}}$ to $X_N = 6 \cdot 10^7$ cm for $U_1 = 15 \ {\rm km \ s^{-1}}$.

In order to solve the radiation transfer equation (54) with the Feautrier technique the slab is divided into $4000 \le N \le 6000$ cells with 1500 cells in the preshock region. The cells are smallest at $X_{\mathcal{J}} = 0$ and increase in both directions from

the discontinuous jump according to the geometrical progression. For all models the cell size at the discontinuous jump is $\Delta X_{\jmath-1/2} = \Delta X_{\jmath+1/2} = 0.1$ cm. The continuum frequency range is divided into $L_{\rm c} = L$ frequency intervals $[\nu_i, \nu_{i-1}]$, where ν_i is the threshold frequency for ionization from the i–th state, $1 \le i \le L$ and $\nu_0 = 10^{16}$ Hz is the the upper boundary of the frequency range. The frequency integrals (63) – (65) were computed using the Gauss–Legendre quadratures with $n_{\rm c} = 12$ nodes for the continuum intervals and with $n_\ell = 11$ nodes for spectral lines. For the angular integration of the Eddington moments (66) – (68) we make use of the Gauss–Legendre quadrature with $n_\mu = 12$ nodes.

In order to consider the dependence of the solution on the number of bound atomic levels L and on the width of the frequency range $[\nu_L, \nu_0]$ we calculated three sequences of the models with $L = L_{\rm c} = 2$, 3 and 4. The unperturbed temperature and density of the ambient hydrogen gas are $T_1 = 6000$K and $\rho_1 = 10^{-10}$ gm cm^{-3}, respectively. These conditions are typical for atmospheres of Cepheids and RR Lyr type variables. The convergence of global iterations is very sensitive to the initial approximation, so that the first model of each sequence with $U_1 = 15$ km s^{-1} (the upstream adiabatic Mach number is $M_1 \approx 1.6$) was computed using the initial LTE approximation with postshock temperatures T_a and $T_{\rm e}$ exponentially decaying with increasing distance from the discontinuous jump over the e–folding distance of 10^6 cm. Each converged model was used as an initial approximation for the following model of higher amplitude. In order to avoid strong initial oscillations of iterated quantities the models were computed with amplitude increment $\Delta U_1 = 1\,{\rm km\,s^{-1}}$. The convergence of global iterations depends also on the size of cells approximating the postshock region, so that is why the shock models were represented by several thousand cells.

Hydrodynamic variables that are most sensitive to the accuracy of the solution are the electron temperature $T_{\rm e}$ and the temperature of heavy particles T_a in the vicinity of the postshock outer boundary as well as the radiation flux $F_{\rm R}$ emergent from the slab. Therefore, the convergence of the solution on the $(k+1)$–th iteration was controlled by the maximum correction of the electron temperature within the slab

$$y_1 = \max_{1\le j\le N+1} \left| 1 - T^{(k)}_{{\rm e}j-1/2} / T^{(k+1)}_{{\rm e}j-1/2} \right| \qquad (71)$$

and by the correction of the radiative flux F_1 emergent from the outer boundary of the preshock region

$$y_2 = \left| 1 - F_1^{(k)} / F_1^{(k+1)} \right| . \qquad (72)$$

If global iterations converge, both y_1 and y_2 exhibit the exponential decay with increasing number of global iterations k. The typical behaviour of y_1 and y_2 is displayed in Fig. 1. After a few hundred iterations these quantities cease to decay and oscillate around the constant average values due to the limited accuracy of computations. In the present study the stability of the converged solution was checked for some models within several thousand iterations.

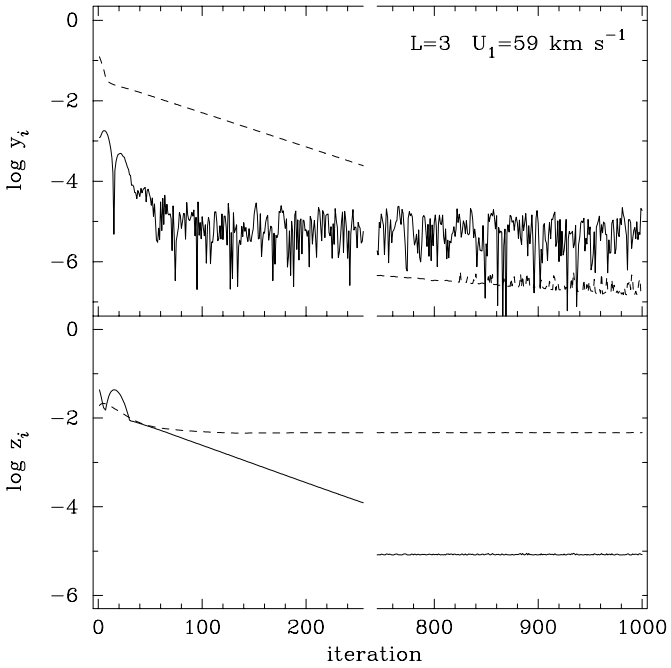

Fig. 1. Convergence plots as a function of the number of global iterations for the model with $U_1 = 59$ km s^{-1}. Upper panel: the maximum corrections of the radiative flux emergent from the slab (solid line) and the electron temperature (dashed line). Lower panel: the maximum relative change of $\mathcal{C}_1$ (solid line) and $\mathcal{C}_2$ (dashed line) throughout the slab.

For controlling the degree of approximation we evaluated also in all cell centers of the model the momentum flux $\mathcal{C}_1$ and the total energy flux $\mathcal{C}_2$ defined by Eqs. (4) and (5), respectively. By definition, both these quantities should remain constant throughout the slab if the solution is exact. On the lower panel of Fig. 1 are shown the maximum deviations

$$z_i = \max_{1\le j\le N+1} \left| 1 - \mathcal{C}_{ij-1/2} / \mathcal{C}_{i1} \right| , \quad (i = 1, 2), \qquad (73)$$

where $\mathcal{C}_{i1}$ are defined at the preshock outer boundary $j = 1$ and $\mathcal{C}_{ij-1/2}$ are defined at the cell centers $1 \le j \le N+1$, respectively. As is seen from the lower panel of Fig. 1, the total energy flux $\mathcal{C}_2$ is constant throughout the slab with errors of less than a few tenths of a percent.

4. General description of models

Shock wave models computed with the same upstream gas temperature T_1 and gas density ρ_1 can be instructively represented by the Hugoniot curve (see, e.g., Zeldovich & Raizer 1966) relating the total pressure P and the specific volume $V = 1/\rho$ just ahead and just behind the discontinuous jump. In our case such a representation can be only approximate because both the gas density and the total pressure ahead the discontinuous jump grow with increasing upstream velocity due to radiative heating in the preshock region. In particular, for upstream velocities $15\ {\rm km\ s^{-1}} \le U_1 \le 70\ {\rm km\ s^{-1}}$ the gas density increases by as much as two percent, whereas the total pressure increases by

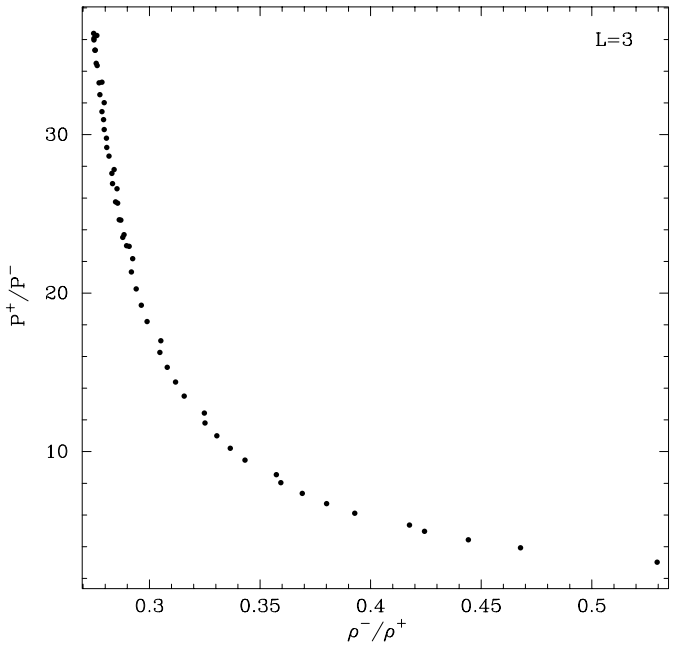

Fig. 2. The pressure ratio P^+/P^- versus the inverse compression $\eta^{-1} = \rho^-/\rho^+$ for models with $L = 3$ and $15\ \mathrm{km\ s^{-1}} \le U_1 \le 70\ \mathrm{km\ s^{-1}}$.

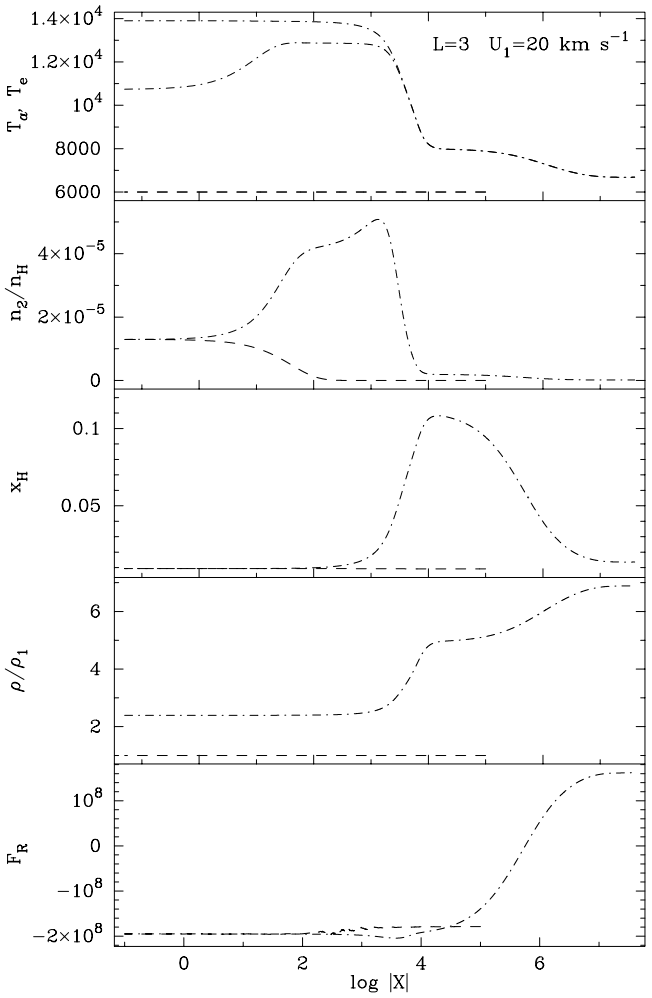

Fig. 3. The electron temperature T_e, the temperature of heavy particles T_a, the ratio of the population number density of the second bound level to the number density of hydrogen atoms n_2/n_H, the degree of hydrogen ionization x_H, the compression ratio ρ/ρ_1, and the total radiative flux F_R versus the distance from the discontinuous jump X for the model with $L = 3$, $U_1 = 20\ \mathrm{km\ s^{-1}}$. In dashed and dot–dashed lines are given the plots for the preshock and postshock regions, respectively.

nearly a factor of three. It should be noted that the growth of the preshock gas density and the gas pressure becomes substantial only at upstream velocities $U_1 > 50\ \mathrm{km\ s^{-1}}$. In comparison with the amplitude of the jump these changes, however, are enough small. The Hugoniot diagram for the sequence of models with $L = 3$ is shown in Fig. 2. The state of the gas at the cell center $X_{\mathcal{J}-1/2}$ is given for all models by $(1, 1)$ and is not shown on the plot. The state of the gas just behind the discontinuous jump at the cell center $X_{\mathcal{J}+1/2}$ is represented for each model by the filled circle.

General properties of converged models computed for $L = 3$ and upstream velocities $U_1 = 20, 40, 60\ \mathrm{km\ s^{-1}}$ are displayed in Figs. 3 – 5, where the electron temperature T_e, the temperature of heavy particles T_a, the ratio of the number density of hydrogen atoms in the second state to the number density of hydrogen atoms n_2/n_H, the hydrogen ionization degree x_H, the compression ratio ρ/ρ_1, and the total radiative flux F_R are shown as a function of the distance from the discontinuous jump X. For the sake of convenience the independent variable X is in logarithmic scale and each plotted variable is represented by two branches corresponding to the preshock and postshock regions, respectively. Just behind the discontinuous jump the temperature of neutral hydrogen atoms and hydrogen ions T_a exceeds the temperature of the electron gas T_e. That is why in the upper panel of Figs. 3 – 5 the postshock temperature plots are represented by two converging curves.

Properties of shock wave models are listed also in Table 1. The column U_1 give the upstream velocity at the outer boundary of the slab, F_R is the radiative flux emergent from the preshock outer boundary and $F_\mathrm{R}/\mathcal{C}_2$ is the ratio of the radiative flux to the total energy flux at the preshock outer boundary. Columns headed by $X_{\mathcal{J}-1/2}$ describe the state of gas just ahead the discontinuous jump. Because in the preshock region the divergence of radiative flux is negative, we use its absolute value $\mathcal{D} = |\nabla \cdot \mathbf{F}_\mathrm{R}|/\rho$. The total rise of the gas temperature and the total rise of the hydrogen ionization degree in the preshock region within the interval $\left[X_1, X_{\mathcal{J}-1/2}\right]$ are given in columns ΔT and Δx_H, respectively. The columns headed by $X_{\mathcal{J}+1/2}$ give the temperature of heavy particles T_a^+, the temperature of the electron gas T_e^+ and the compression ratio $\eta = \rho^+/\rho^-$ just behind the discontinuous jump at the cell center $X_{\mathcal{J}+1/2}$. The columns headed by $\max \mathcal{D}$ give the maximum value of the divergence of radiative flux in the postshock region (in these layers $\nabla \cdot \mathbf{F}_\mathrm{R} > 0$) and the space coordinate X where this maximum is attained. The last two columns are headed by $\max x_\mathrm{H}$ and give the maximum ionization degree of hydrogen x_H in the

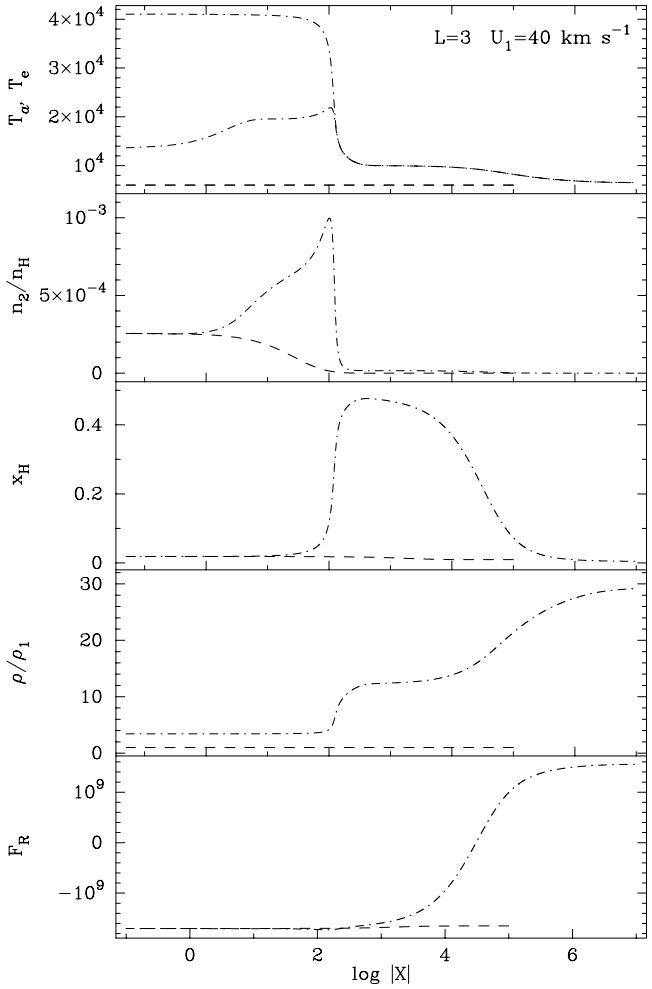

Fig. 4. Same as Fig. 3 for model with $L = 3$, $U_1 = 40$ km s^{-1}.

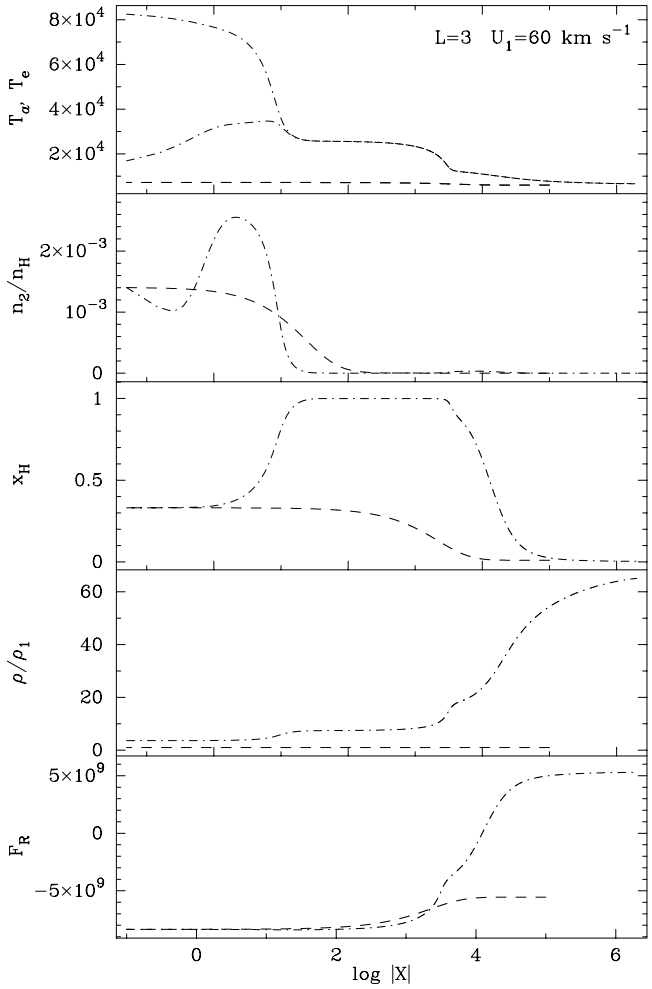

Fig. 5. Same as Fig. 3 for model with $L = 3$, $U_1 = 60$ km s^{-1}.

postshock region as well as the distance X of this maximum from the discontinuous jump.

A cursory inspection of Table 1 shows that the total radiative flux $F_{\rm R}$ nearly does not depend on the number of bound atomic levels L. In other words, the radiative flux emergent from the shock wave is independent of the lower limit ν_L of the frequency range provided that $\nu_L < \nu_2$. At the same time, the change of ν_L is accompanied by redistribution of the energy of radiation field within $[\nu_L, \nu_0]$ which is most perceptible within the Lyman continuum In particular, for the narrower frequency range (e.g. for $L = 2$) we have both stronger radiative heating and higher hydrogen ionization in the preshock region. The structure of the postshock region is also sensitive to the width of the frequency range $[\nu_L, \nu_0]$. In particular, for the narrower frequency range the thermal equipartition and the maximum of ionization are attained at larger distances from the discontinuous jump.

5. Radiation field

We consider the shock waves propagating through the partially ionized hydrogen gas which is opaque both in the Lyman continuum and in the Lyman lines. The total optical depth of the slab at the frequency ν_1 corresponding to the threshold ionization from the ground state is in the range $10^4 \lesssim \tau(\nu_1) \lesssim 10^5$, the maximum $\tau(\nu_1) \sim 10^5$ being reached at $U_1 \approx 40$ km s^{-1}. At the same time the slab is nearly transparent for continuum radiation at frequencies $\nu < \nu_1$. The optical depths in the centers of Balmer lines are $\tau_\nu \ll 1$ in the preshock region and gradually increase with increasing distance from the discontinuous jump in the postshock region. At distances $X \gtrsim 10^4$ cm the postshock optical depth in the center of the Hα spectral line measured from the discontinuous jump is $\tau_\nu \gtrsim 1$. In Fig. 6 we give the plots of monochromatic optical depths τ_ν measured from the discontinuous jump to the layer with space coordinate X for the heads of continua with threshold frequencies ν_i $(1 \le i \le 3)$ and for the centers of spectral lines Lyα and Hα.

Thus, the Eddington approximation cannot be applied for the solution of the radiation transfer problem in shock waves. Indeed, it is valid only within the Lyman continuum whereas the most of radiation is transported at frequencies lower than the Lyman edge where the angular dependence of the specific intensity $I_{\mu\nu}$ must be taken into account. Moreover, the correct calculation of the angular dependence of the specific intensity $I_{\mu\nu}$ is of great importance because for $\nu < \nu_1$ the term

Table 1. Parameters of shock wave models with $\rho_1 = 10^{-10}$ gm cm^{-3} and $T_1 = 6000$K.

				$X_{\mathcal{J}-1/2}$			$X_{\mathcal{J}+1/2}$			$\max \mathcal{D}$		$\max x_{\rm H}$	
U_1	M_1	$\log F_{\rm R}$	$F_{\rm R}/\mathcal{C}_2$	$\log \mathcal{D}$	ΔT	$\Delta x_{\rm H}$	T_a^+	$T_{\rm e}^+$	ρ^+/ρ^-	$\log \mathcal{D}$	$\log X$	$x_{\rm H}$	$\log X$
$L = 2$													
15	1.64	7.736	0.176	12.35	0	0.000	9853	9134	1.878	12.034	4.49	0.06	4.96
20	2.18	8.268	0.392	13.34	0	0.000	13970	10890	2.445	12.759	3.92	0.11	4.24
25	2.73	8.593	0.551	14.04	0	0.001	19113	12038	2.842	13.285	3.39	0.18	3.74
30	3.28	8.846	0.678	14.52	0	0.002	25337	12801	3.116	13.749	2.97	0.26	3.38
35	3.82	9.039	0.731	14.89	3	0.005	32661	13329	3.308	14.118	2.67	0.36	3.10
40	4.37	9.218	0.802	15.23	14	0.010	41084	13717	3.444	14.387	2.46	0.47	2.84
45	4.91	9.369	0.836	15.56	40	0.019	50582	14034	3.542		1.89	0.61	2.59
50	5.46	9.509	0.880	15.93	112	0.041	61069	14379	3.608		1.64	0.76	2.40
55	6.00	9.635	0.918	16.34	405	0.122	72054	15129	3.631		1.26	0.94	2.30
60	6.55	9.746	0.929	16.65	1617	0.366	81868	17740	3.554		0.38	1.00	1.62
65	7.08	9.844	0.918	16.65	3527	0.648	90756	21691	3.435		0.34	1.00	1.24
70	7.58	9.949	0.968	16.33	5029	0.862	100569	24765	3.365		0.30	1.00	1.06
$L = 3$													
15	1.64	7.794	0.199	12.34	0	0.000	9866	9166	1.888	12.196	4.46	0.05	4.93
20	2.18	8.272	0.386	13.24	0	0.000	13900	10739	2.395	12.900	3.79	0.11	4.17
25	2.73	8.593	0.539	13.91	0	0.001	19051	11913	2.798	13.491	3.19	0.18	3.62
30	3.28	8.843	0.657	14.35	2	0.002	25283	12704	3.079	13.961	2.79	0.26	3.22
35	3.82	9.039	0.720	14.68	7	0.005	32614	13253	3.277	14.291	2.52	0.36	2.90
40	4.37	9.218	0.790	14.98	16	0.009	41041	13654	3.419	14.525	2.32	0.48	2.63
45	4.91	9.368	0.826	15.29	39	0.018	50541	13976	3.521	14.701	2.17	0.61	2.41
50	5.46	9.513	0.887	15.62	102	0.041	61026	14310	3.591	14.861	2.09	0.77	2.24
55	6.00	9.630	0.891	16.03	327	0.117	72040	14919	3.621		2.26	0.95	2.18
60	6.55	9.744	0.916	16.43	1203	0.321	82504	16849	3.578		3.46	1.00	1.57
65	7.08	9.846	0.924	16.59	2651	0.541	92943	19958	3.504		4.11	1.00	1.20
70	7.58	9.970		16.51	4107	0.748	103543	23023	3.438		4.55	1.00	1.02
$L = 4$													
15	1.64	7.755	0.176	12.26	0	0.000	9716	8886	1.803	12.240	4.49	0.05	4.97
20	2.18	8.276	0.385	13.14	0	0.000	13866	10667	2.371	12.967	3.77	0.11	4.16
25	2.73	8.587	0.521	13.79	0	0.001	19023	11854	2.777	13.556	3.16	0.18	3.59
30	3.28	8.835	0.633	14.24	3	0.002	25347	12827	3.124	14.020	2.75	0.26	3.18
35	3.82	9.040	0.717	14.55	7	0.005	32592	13215	3.263	14.329	2.51	0.36	2.86
40	4.37	9.210	0.761	14.85	16	0.009	41022	13622	3.407	14.557	2.30	0.48	2.59
45	4.91	9.372	0.835	15.16	38	0.018	50524	13948	3.510	14.729	2.14	0.61	2.38
50	5.46	9.504	0.851	15.51	99	0.040	61089	14365	3.614	14.889	2.05	0.77	2.21
55	6.00	9.630	0.884	15.94	297	0.113	72061	14837	3.616		2.23	0.95	2.16
60	6.55	9.743	0.909	16.38	1069	0.302	82746	16553	3.584		3.41	1.00	1.56
65	7.08	9.847	0.923	16.58	2377	0.503	93630	19398	3.524		4.04	1.00	1.19
70	7.58	9.973		16.57	3772	0.696	104720	22378	3.466		4.47	1.00	1.01

$$\frac{1}{\mu}\int\limits_0^{\tau_\nu} S_\nu(t) e^{-(t-\tau_\nu)/\mu} dt \tag{74}$$

rapidly decreases for $\mu \to |1|$ and the Eddington factor is $f_\nu = K_\nu/J_\nu < 1/3$.

The interaction between the radiation field and the gas material is described in terms of the divergence of radiative flux $\nabla \cdot \mathbf{F}_{\rm R}$. By definition, this quantity is negative when the gas absorbs more energy than it emits, whereas when $\nabla \cdot \mathbf{F}_{\rm R} > 0$, the gas radiatively cools. The typical plot of the divergence of radiative flux expressed per unit mass $\frac{1}{\rho}\nabla \cdot \mathbf{F}_{\rm R}$ is shown on the upper panel of Fig. 7 for the shock wave model with $L = 3$ and $U_1 = 40$ km s^{-1}. The gradual decrease of $\frac{1}{\rho}\nabla \cdot \mathbf{F}_{\rm R}$ in the preshock region is due to the strong absorption of the Lyman continuum radiation which leads to the growth of the gas temperature when the parcel of gas approaches the discontinuous jump. The heating of gas rapidly increases with increasing upstream velocity and as is seen from Table 1 the quantity $\mathcal{D} = |\nabla \cdot \mathbf{F}_{\rm R}|/\rho$ at $X_{\mathcal{J}-1/2}$ changes be several orders of magnitude for 15 km s$^{-1} \le U_1 \le 70$ km s^{-1}.

The jump of $\frac{1}{\rho}\nabla \cdot \mathbf{F}_{\rm R}$ within $[X_{\mathcal{J}-1/2}, X_{\mathcal{J}+1/2}]$ is due to the adiabatic heating of electrons at the discontinuous jump. The layers of the most efficient radiative cooling in the postshock region with fastest decrease of the gas temperature are revealed

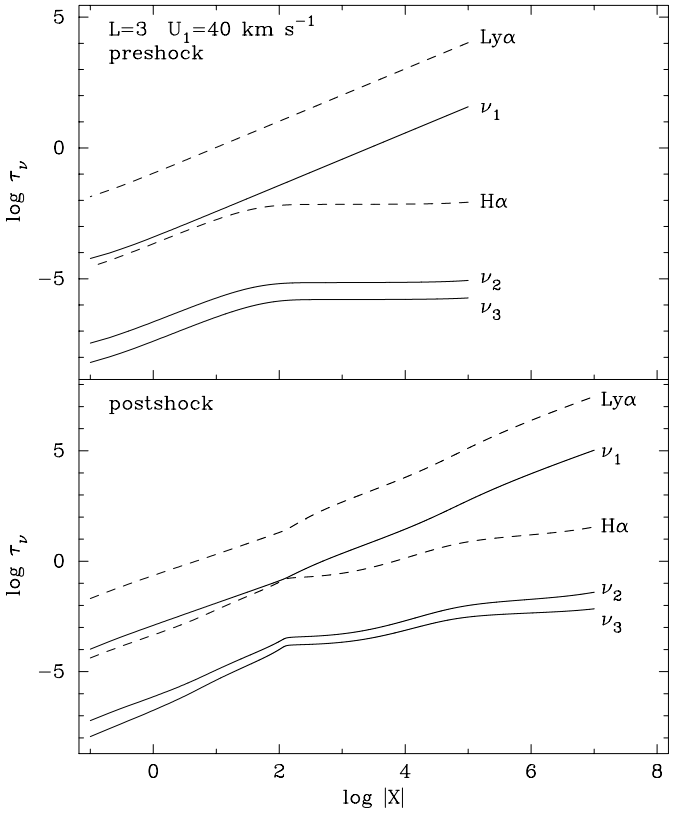

Fig. 6. Monochromatic optical depths τ_ν measured from the discontinuous jump for the preshock (upper panel) and postshock (lower panel) regions of the model with $L = 3, U_1 = 40\ \mathrm{km\ s^{-1}}$. In solid lines are shown the optical depths at the heads of the continua and in dashed lines are shown the optical depths at the centers of spectral lines.

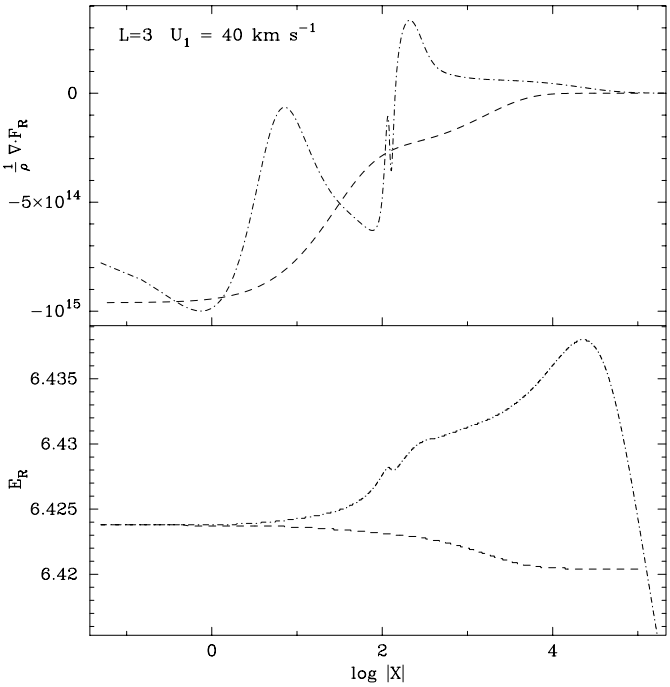

Fig. 7. The divergence of radiative flux per unit mass (upper panel) and the radiation energy density (lower panel) as a function of the distance from the discontinuous jump for the model with $L = 3, U_1 = 40\ \mathrm{km\ s^{-1}}$. In dashed and dot–dashed lines are given the preshock and postshock plots, respectively.

by the maximum of $\frac{1}{\rho}\nabla\cdot\mathbf{F}_\mathrm{R}$ which also very rapidly increases with increasing U_1 (see Table 1). The divergence of radiative flux approaches zero with increasing distance from the discontinuous jump in the both preshock and postshock regions. This implies that at large distances from the discontinuous jump the total radiative flux F_R tends to be constant.

While the parcel of gas approaches the discontinuous jump in the preshock region the radiation energy density E_R gradually increases due to the radiative heating of gas. Behind the discontinuous jump E_R continues to increase and reaches the maximum in the layers of the fastest recombination of hydrogen atoms. The maximum of the radiation energy density E_R in the postshock region approximately corresponds to the point where the total radiative flux is $F_\mathrm{R} = 0$. It should be noted, however, that this condition is exact only in the diffusion approximation (see, e.g., Mihalas & Mihalas 1984) and as is shown below the space coordinate of the layer with $F_\nu = 0$ depends on the frequency ν. The typical plot of E_R is shown on the lower panel of Fig. 7. For all models considered in the present study the radiation energy density E_R can be neglected in comparison with the thermal energy of the gas. For example, in the model represented in Fig. 7 the ratio of the radiation energy density to the enthalpy is $E_\mathrm{R}/h \lesssim 10^{-3}$ throughout the whole shock wave.

The radiative flux outgoing from the preshock outer boundary is nearly the same as that outgoing from the postshock outer boundary, that is, $-F_1 \approx F_N$. The radiative flux emergent from the shock wave rapidly increases with increasing upstream velocity and at $U_1 \approx 60\ \mathrm{km\ s^{-1}}$ more than 90 percent of the total energy flux is contained in the radiation flux. As is seen from Fig. 8 where we give the plot of the ratio $F_\mathrm{R}/\mathcal{C}_2$ versus the upstream velocity U_1, at upstream Mach numbers $M_1 \gtrsim 6$ the major part of the shock wave energy (i.e. more than 90%) is lost due to radiation.

At upstream velocities $U_1 < 40\ \mathrm{km\ s^{-1}}$ the total radiative flux is nearly constant in the preshock region and undergoes the substantial changes only behind the discontinuous jump in the layers where the gas radiatively cools and recombines. However the role of the Lyman continuum radiation rapidly increases with increasing upstream velocity and for $U_1 > 40\ \mathrm{km\ s^{-1}}$ the total radiative flux F_R shows perceptible changes in the preshock region (see Fig. 5).

Of great interest are the spectral distributions of monochromatic quantities describing the radiation field as a function of frequency ν. In Fig. 9 we give the spectra of monochromatic radiative flux F_ν for three different layers: the preshock outer boundary X_1, the discontinuous jump $X_\mathcal{J}$ and the postshock outer boundary X_N in the model with $L = 3$ and $U_1 = 40\ \mathrm{km\ s^{-1}}$. As is seen from these plots, the most of radiation is transported within the frequency interval $\nu_2 < \nu < \nu_1$ limited by the edges of the Balmer and Lyman continua. The

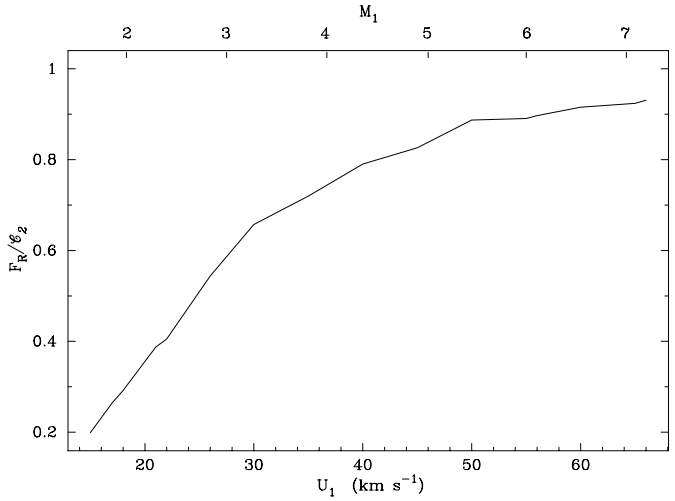

Fig. 8. The ratio of the radiative flux $F_{\rm R}$ emergent from the preshock outer boundary to the total energy of the shock wave $\mathcal{C}_2$ versus the upstream gas flow velocity U_1 for models with $L = 3$. Along the upper horizontal axis are given the upstream adiabatic Mach numbers M_1.

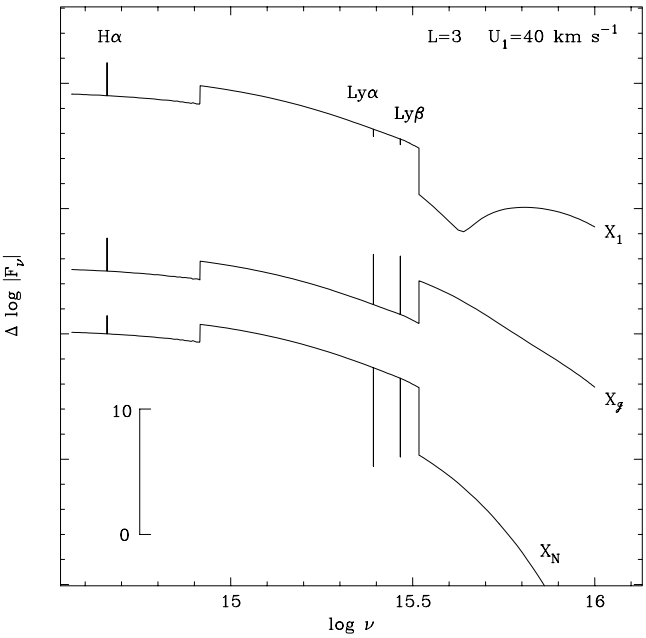

Fig. 9. Monochromatic radiative flux F_ν as a function of frequency ν for the preshock outer boundary X_1, discontinuous jump $X_\jmath$ and postshock outer boundary X_N. For the sake of convenience the plots are arbitrarily shifted along the vertical axis.

contribution of the Lyman continuum radiation is perceptible only in the vicinity of the discontinuous jump.

The conspicuous feature of these plots is also that the Hα spectral line is in emission throughout the shock wave, whereas the Lyα and Lyβ lines are mostly in absoprtion and are revealed in emission only in the vicinity of the discontinuous jump. Within the range of upstream velocities $15\ \mathrm{km\ s^{-1}} \le U_1 \le 70\ \mathrm{km\ s^{-1}}$ the frequency dependencies of the radiative flux are qualitatively similar to that shown in Fig. 9.

The role of various spectral intervals in the total radiation transfer can be evaluated with use of terms

$$F_i^c = 4\pi \int\limits_{\nu_i}^{\nu_{i-1}} H_\nu d\nu \tag{75}$$

and

$$F_i^\ell = 4\pi \int\limits_{\nu_i-\Delta\nu_i}^{\nu_i+\Delta\nu_i} H_\nu d\nu \tag{76}$$

representing the radiative flux integrated within the continuum frequency intervals $[\nu_i, \nu_{i-1}]$ and within the spectral lines, respectively. Here $\Delta\nu_i$ is the half–width of the spectral line frequency interval. Figs. 10 – 12 show F_i^c and F_i^ℓ as a function of the distance from the discontinuous jump for models with $U_1 = 20$, 40 and $60\ \mathrm{km\ s^{-1}}$, respectively. For the sake of convenience of the graphical representation the fluxes are given in the logarithmic scale. As is seen from these plots throughout the shock wave the most of radiation is transported within the Balmer continuum. The role of the Lyman continuum becomes perceptible at upstream velocities $U_1 > 40\ \mathrm{km\ s^{-1}}$ only in the vicinity of the discontinuous jump: $-10^4\ \mathrm{cm} \lesssim X \lesssim 10^4\ \mathrm{cm}$. In the preshock region the radiative flux is constant at frequencies $\nu < \nu_1$. The Lyman continuum flux ($\nu_1 \le \nu \le \nu_0$) rapidly increases with approaching the discontinuous jump and becomes perceptible at distances smaller than $X \sim 10^4\ \mathrm{cm}$. But even in the vicinity of the discontinuous jump the radiative energy transport in the Lyman continuum remains small in comparison with that at lower frequencies until the upstream velocity is $U_1 \lesssim 40\ \mathrm{km\ s^{-1}}$.

As is seen from the plots given on the lower panels of Figs. 10 – 12 the contribution of the spectral line radiation into the total radiative flux is negligible. Throughout the slab the most of the spectral line radiation is transported by Hα and only at upstream velocities $U_1 > 50\ \mathrm{km\ s^{-1}}$ in the close vicinity of the discontinuous jump the spectral line radiation is transported mostly in Lyα.

Behind the discontinuous jump the monochromatic radiative flux undergoes substantial changes within the radiative cooling region from where the most of radiation is emerged in both opposite directions. By definition, the monochromatic radiative flux changes its sign in the layer where $\nabla\cdot\mathbf{F}_\nu$ reaches the maximum. In plots given in Figs. 10 – 12 these layers are revealed as deep maxima of the continuum and spectral line fluxes F_i^c and F_i^ℓ, respectively.

As is seen, the region emerging radiation is spread along the space coordinate in wide ranges: $3.8 \lesssim \log X \lesssim 6.5$ for $U_1 = 20\ \mathrm{km\ s^{-1}}$ and $3.5 \lesssim \log X \lesssim 4.1$ for $U_1 = 60\ \mathrm{km\ s^{-1}}$. This is obviously due to strong frequency dependence of optical depths τ_ν in layers emitting the radiation.

6. Preshock region

Effects of the electron thermal conduction in the vicinity of the discontinuous jump are not considered in the present study,

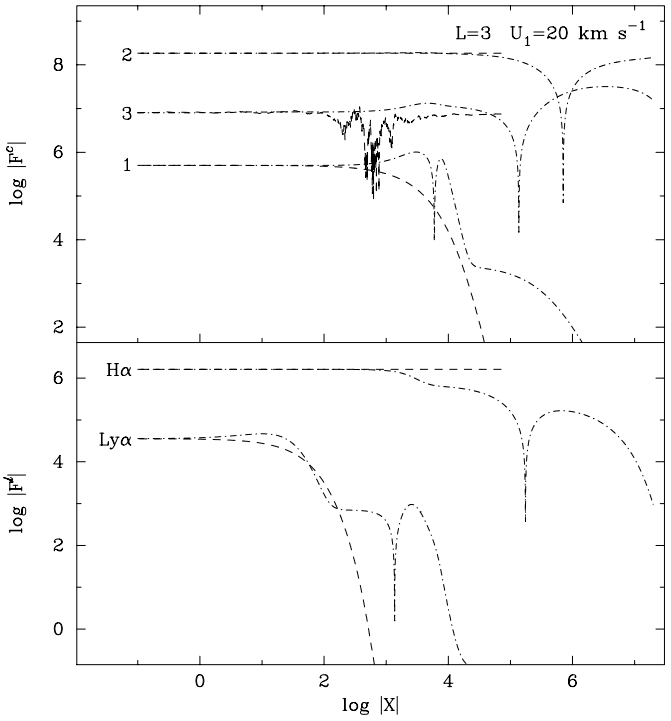

Fig. 10. The radiative flux in continuum intervals F_i^c (upper panel) and in spectral lines (lower panel) for model with $L = 3, U_1 = 20\,\mathrm{km\,s^{-1}}$. In dashed and dot–dashed lines are represented the preshock and postshock plots, respectively.

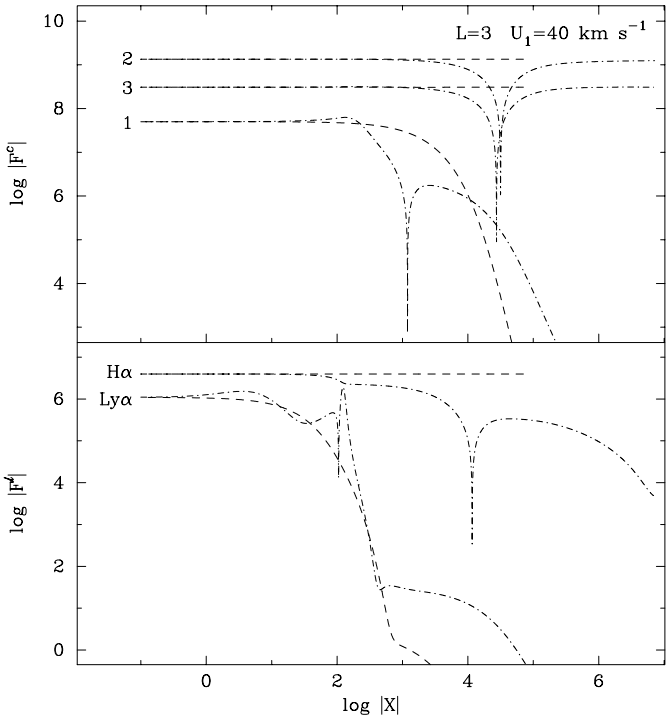

Fig. 11. Same as Fig. 10 for model with $L = 3, U_1 = 40\,\mathrm{km\,s^{-1}}$.

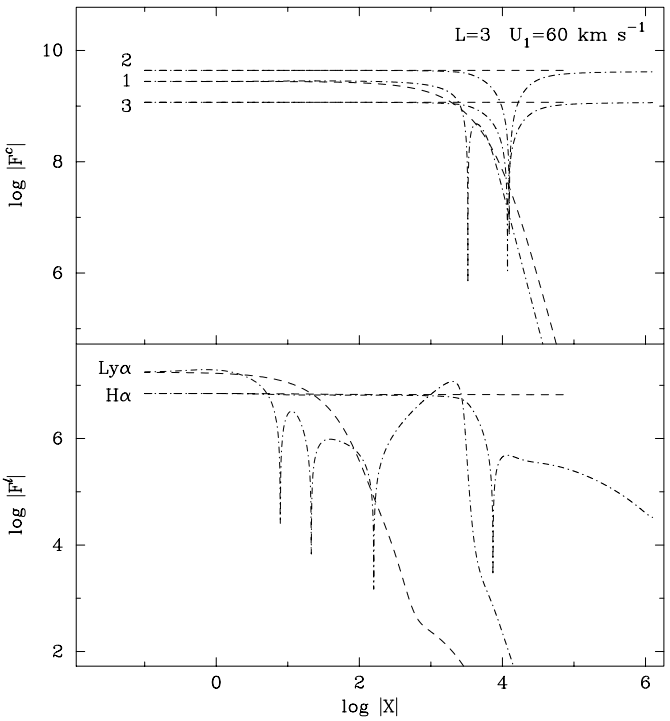

Fig. 12. Same as Fig. 10 for model with $L = 3, U_1 = 60\,\mathrm{km\,s^{-1}}$.

therefore throughout the preshock region the translational energies of the both hydrogen atoms and free electrons are equal and can be described in terms of the gas temperature: $T = T_a = T_\mathrm{e}$. For $T = 6000\mathrm{K}$ and $\rho = 10^{-10}\,\mathrm{gm\,cm^{-3}}$ most of the hydrogen atoms are in the ground state, so that the zone in which the radiation field interacts with gas material is only of several mean free paths of photons at the frequency of the Lyman continuum edge ν_1. For our models this corresponds to the distance from the discontinuous jump of $X \sim 10^4\,\mathrm{cm}$. Within this zone known as the radiative precursor the gas undergoes both radiative heating and photoionization. The rize of the gas temperature ΔT and the hydrogen ionization degree Δx_H within the preshock region is nearly negligible in shocks with upstream velocities smaller than $U_1 \approx 30\,\mathrm{km\,s^{-1}}$ but at larger upstream velocities ΔT and Δx_H very rapidly grow with increasing U_1 (see Table 1). At upstream velocities $U_1 > 65\,\mathrm{km\,s^{-1}}$ the hydrogen ionization degree ahead the discontinuous jump is $x_\mathrm{H} > 0.5$ and the gas material becomes more transparent. This accounts for the small decrease of $\mathcal{D} = |\nabla\cdot\mathbf{F}_\mathrm{R}|/\rho$ for $U_1 > 65\,\mathrm{km\,s^{-1}}$.

Throughout the preshock region the collisional ionizations can be neglected since their rates are by several orders of magnitude smaller than those of photoionizations. In Fig. 13 we give the plots of the net rates of radiative ionizations

$$Z_{i\kappa} = n_i R_{i\kappa} - n_\mathrm{e}\frac{n_i^*}{n_\kappa^*}R_{i\kappa}^\dagger \tag{77}$$

for first three atomic levels in models with $U_1 = 20$, 40 and $60\,\mathrm{km\,s^{-1}}$. At distances from the discontinuous jump less than $X \sim 10^2\,\mathrm{cm}$ the absorption coefficient in Lyα and Lyβ lines exceeds that of the Lyman continuum. For upstream velocities $U_1 < 30\,\mathrm{km\,s^{-1}}$ the ionization from the ground state is still small and in layers with $X < 10^2\,\mathrm{cm}$ the hydrogen ionizes mostly from excited levels $i \geq 2$. However the rapid growth of the ionization from the ground state with increasing upstream

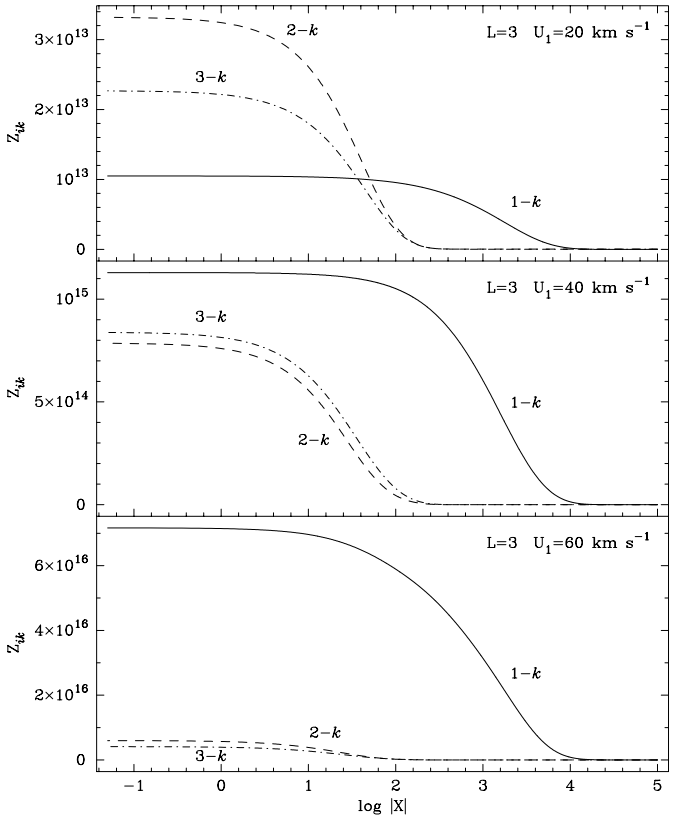

Fig. 13. Net radiative ionization rates for the ground state (solid line), second level (dashed line) and third level (dot–dashed line) in the preshock regions of the shock wave models with $U_1 = 20$ km s^{-1} (upper panel), $U_1 = 40$ km s^{-1} (middle panel) and $U_1 = 60$ km s^{-1} (lower panel).

velocity cancels this effect and at $U_1 > 30\,\mathrm{km\,s^{-1}}$ the hydrogen ionizes mostly from the ground state.

The columns ΔT and Δx_H of Table 1 give the total growth of the gas temperature and ionization degree in the preshock region. As is seen, at constant upstream velocity U_1 both ΔT and Δx_H decrease for larger L. As was noted above the total radiative flux emitted by the shock wave nearly does not depend on the frequency range $[\nu_L, \nu_0]$ for $L > 2$ and for smaller ν_L the monochromatic flux is redistributed among lower frequencies. In particular, the fraction of the Lyman continuum radiation in the total radiative flux decreases.

The heating of the gas within the radiative precursor is accompanied by the rise of the gas pressure P_g and the gas density ρ. However the increase of ρ is not large and for $U_1 = 60$ km s^{-1} the gas density just ahead the discontinuous jump is $\rho^- = 1.0085\rho_1$, so that the upstream gas flow velocity decreases by less than one per cent and is $U^- = 0.9916U_1$. More important is the rise of the gas temperature T because it leads to the slow decrease of the compression ratio ρ^+/ρ^- with increasing U_1 in shocks with upstream velocities $U_1 > 55$ km s^{-1} (see Table 1). Such a decrease of the compression ratio ρ^+/ρ_1 with increasing upstream velocity is easily explained in terms of the Rankine–Hugoniot relations (3) – (5). Adopting $F_\mathrm{R}^- = F_\mathrm{R}^+$ in (11) and neglecting the contribution of the radiation energy density E_R and radiation pressure P_R in Eqs. (11) and (12) we find that the compression ratio at the discontinuous jump is

$$\frac{\rho^+}{\rho^-} = \frac{4\,(U^-)^2}{5\,\left(a_\mathrm{T}^-\right)^2 + (U^-)^2}. \tag{78}$$

Thus, the slow decrease of the compression ratio ρ^+/ρ^- with increasing U_1 is due to the rize of the isothermal sound speed ahead the discontinuity jump. Inspection of Table 1 shows that the effect of decreasing ρ^+/ρ^- becomes less prominent in the models computed with larger L and, therefore, having somewhat weaker radiative heating of the gas just ahead the discontinuous jump.

For gas densities of $10^{-14}\,\mathrm{g\,cm^{-3}} \lesssim \rho \lesssim 10^{-8}\,\mathrm{g\,cm^{-3}}$ the dominant recombination mechanism is the three–body recombination (see, e.g., Zeldovich & Raizer 1967) and as was shown by Gillet & Lafon (1990) the precursor heating is due to the partial transformation of the ionization energy into the thermal energy via the three–body recombination processes. Kuznetsov & Raizer (1965) have shown that electrons are captured on the level with energy $U_i = \chi_\mathrm{H}/i^2$ close to the average kinetic energy of free electrons kT_e. Thus, $i = \sqrt{\chi_\mathrm{H}/kT_\mathrm{e}}$ and for the precursor temperature range $6000\mathrm{K} \le T_\mathrm{e} \lesssim 10^4\mathrm{K}$ (see Table 1) the free electrons should be captured onto levels $4 \le i \le 5$. Thus, the atomic model represented by 4 bound levels seems not to underestimate significantly the rates of three–body recombinations and, therefore, the precursor heating is treated quite correctly. This conclusion is consistent with the decrease of the temperature rize ΔT obtained for atomic models with $L = 3$ and $L = 4$ (see Table 1).

7. Postshock region

Just behind the discontinuous jump the temperature of neutral hydrogen atoms and hydrogen ions T_a^+ exceeds the temperature of free electrons T_e^+ (see Table 1) and as is seen from Figs. 3 – 5 both these temperatures tend to equalize with increasing distance X. Together with excitation of bound atomic levels the thermal equilibration is the fastest relaxation process behind the discontinuous jump. For the models considered in the present study the hydrogen ionization degree ahead the discontinuous jump is $x_\mathrm{H}^- > 10^{-2}$, so that ionized hydrogen atoms are numerous enough behind the discontinuous jump and free electrons gain the energy from heavy particles mostly in elastic collisions with hydrogen ions. It should be noted that for all models throughout the postshock region $Q_\mathrm{ei} \gg Q_{ea}$.

When the temperatures of heavy particles and free electrons equalize, the gas radiatively cools and the gas temperature $T = T_a = T_\mathrm{e}$ gradually decreases with increasing distance from the discontinuous jump. The radiative cooling is fastest when the divergence of radiative flux (47) reaches its maximum. The maximum postshock values of $\frac{1}{\rho}\nabla\cdot\mathbf{F}_\mathrm{R}$ and the space coordinate X, where this maximum is reached, are given in Table 1. The maximum of $\frac{1}{\rho}\nabla\cdot\mathbf{F}_\mathrm{R}$ is prominent only when the postshock ionization degree is $x_\mathrm{H} < 0.8$ and for larger x_H the spatial dependence of $\frac{1}{\rho}\nabla\cdot\mathbf{F}_\mathrm{R}$ shows the plateau rather than the maximum. It should be noted that the maximum of $\nabla\cdot\mathbf{F}_\mathrm{R}$ gives

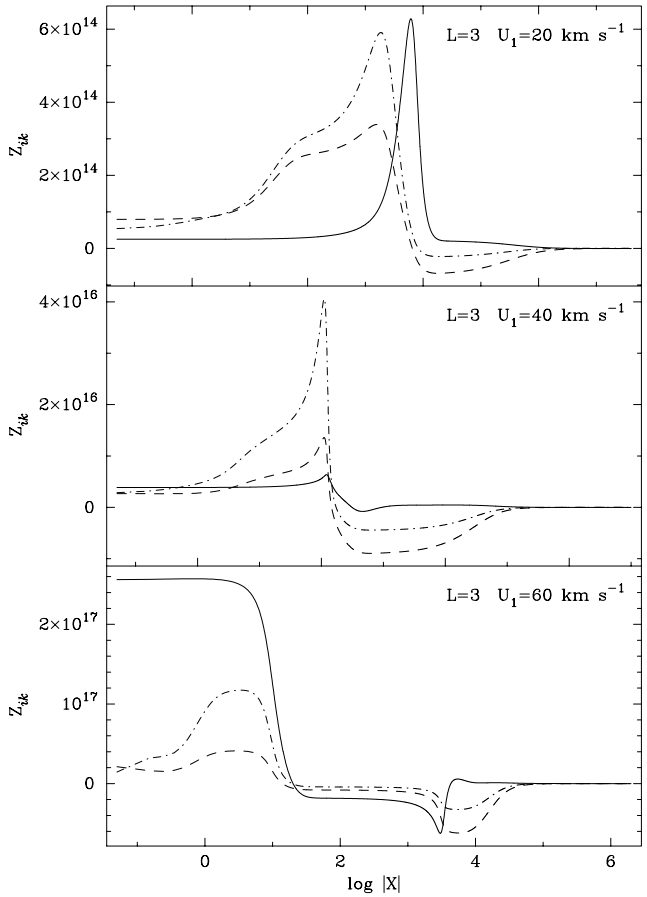

Fig. 14. Net radiative ionization rates from the ground state (solid line), from the second level (dashed line) and from the third level (dot–dashed line) in the postshock region of the shock wave models with $U_1 = 20\ \mathrm{km\ s^{-1}}$ (upper panel), $U_1 = 40\ \mathrm{km\ s^{-1}}$ (middle panel) and $U_1 = 60\ \mathrm{km\ s^{-1}}$ (lower panel).

only the frequency averaged location of the layers emitting the radiation. As was shown above the space coordinate of these layers depends on the frequency of radiation ν.

The ionization of hydrogen atoms is the slower relaxation process in comparison with thermal equilibration and the maximum of x_H is reached behind the maximum of $\frac{1}{\rho}\nabla\cdot\mathbf{F}_\mathrm{R}$ (see Table 1). Throughout the postshock region the rates of collisional processes are by several orders of magnitude smaller than those of radiative processes and, therefore, can be neglected. Fig. 14 shows the net photoionization rates $Z_{i\kappa}$ for the first three bound levels of the hydrogen atom in models with $U_1 = 20$, 40 and $60\ \mathrm{km\ s^{-1}}$. In the postshock region the bound atomic levels are excited faster than hydrogen ionizes, so that at upstream velocities $U_1 < 50\ \mathrm{km\ s^{-1}}$ hydrogen atoms ionize mostly from bound levels $i \geq 2$. At upstream velocities $U_1 > 55\ \mathrm{km\ s^{-1}}$ more than ten percent of hydrogen ionizes in the precursor and in the postshock region the hydrogen ionizes mostly from the ground state. At $U_1 > 55\ \mathrm{km\ s^{-1}}$ the maximum postshock ionization degree is $x_\mathrm{H} \approx 1$. This leads to the slower postshock temperature decrease until the hydrogen ionization degree is near the maximum (see the upper panel of Fig. 5).

The full thickness of the relaxation zone behind the discontinuous jump is determined by the slowest relaxation process which in our case is the recombination of hydrogen atoms. Substitution of the translational energies of hydrogen atoms and free electrons $\widetilde{E}_\mathrm{t} = \widetilde{E}_a + \widetilde{E}_\mathrm{e}$ into the Rankine–Hugoniot equations (4) and (5), where we neglect terms with E_R and P_R, gives

$$\left(\widetilde{E}_\mathrm{t} - \widetilde{E}_{\mathrm{t}1}\right) + \left(\widetilde{E}_\mathrm{ex} - \widetilde{E}_{\mathrm{ex}1}\right) + \left(\widetilde{E}_\mathrm{I} - \widetilde{E}_{\mathrm{I}1}\right) = \\ = \frac{1}{2}\left(P_\mathrm{g} + P_{\mathrm{g}1}\right)\frac{\eta - 1}{\rho} + \frac{F_{\mathrm{R}1} - F_\mathrm{R}}{\dot{m}}. \tag{79}$$

Here subscript 1 denotes the quantities defined at the preshock outer boundary X_1. For strong shock waves with $\widetilde{E}_{\mathrm{t}1} \ll \widetilde{E}_\mathrm{t}$, $\widetilde{E}_{\mathrm{ex}1} \ll \widetilde{E}_\mathrm{ex}$ and $\widetilde{E}_{\mathrm{I}1} \ll E_\mathrm{I}$ the relation (79) is rewritten as

$$\eta = 4 + 3\frac{\widetilde{E}_\mathrm{ex} + \widetilde{E}_\mathrm{I}}{\widetilde{E}_\mathrm{t}} + 3\frac{F_\mathrm{R} - F_{\mathrm{R}1}}{\dot{m}\widetilde{E}_\mathrm{t}}. \tag{80}$$

The first term in (80) is the limiting compression ratio $(\gamma + 1)/(\gamma - 1) = 4$ for the strong adiabatic shock front ($M_1 \gg 1$). In fact, because of radiative processes in the precursor the compression ratio at the adiabatic shock front of our models is as large as $\rho^+/\rho^- = 3.6$ (see Table 1). The second and the third terms in (80) describe the additional gas compression which occurs behind the discontinuous jump in the postshock region due to excitation, ionization and recombination of hydrogen atoms. It should be noted that because $F_{\mathrm{R}1} < 0$, the third term in (80) is always positive. Thus, the transfer of the part of the gas flow kinetic energy into internal degrees of freedom of atoms and into radiation field produces the gas density increase behind the discontinuous jump which is much larger than that at the adiabatic shock front. For example, in the model with $U_1 = 60\ \mathrm{km\ s^{-1}}$ we obtained the final compression ratio as high as $\rho/\rho_1 \approx 65$ (see Fig. 5) which approaches the maximum compression ratio of $\gamma M_1^2 \approx 84$ in the isothermal shock wave where all the shock energy is transformed into the radiation.

8. Conclusion

In the work presented here we have substantially improved the computer code for calculating the structure of radiative shock wave models and considered almost the entire zone of postshock hydrogen recombination in shock wave models with upstream Mach numbers $1.6 \leq M_1 \leq 7.5$. This allowed us to obtain the reliable estimates of the radiative flux emitted by the shock wave as a function of the upstream gas flow velocity. The most striking result of our calculations is that the ratio of the radiative flux to the total energy flux of the shock wave very rapidly enlarges with increasing upstream velocity, so that for adiabatic Mach numbers $M_1 > 7$ (i.e. at $U_1 > 65\ \mathrm{km\ s^{-1}}$) the major part of the shock wave energy (more than 90%) is irreversibly lost due to dissipation processes.

Another noteworthy feature of our results is the negligible role of collisional processes in the both bound–bound and bound–free transitions in comparison with radiative transitions throughout the whole shock wave. This circumstance makes our

models independent of uncertainties in cross sections of collisional processes.

The results described in the present paper were obtained for the only case with gas temperature $T_1 = 6000\mathrm{K}$ and gas density $\rho_1 = 10^{-10}\ \mathrm{gm\,cm^{-3}}$ of the ambient unperturbed medium which is most typical for atmospheres of classical Cepheids and RR Lyr type variables. Obviously, many more models have to be constructed for various gas temperatures and gas densities in order to more clearly understand the properties of radiative shock waves observed in astrophysical phenomena. Of particular interest are the gas temperatures and gas densities typical for pulsating late–type stars possessing strong shock–driven stellar winds. The efforts of further calculations will be also directed to the more accurate modelling of strong shock waves in order to consider in detail the run of the ratio $F_\mathrm{R}/\mathcal{C}_2$ as a function of the upstream velocity at Mach numbers $M_1 > 7$.

Acknowledgements. The work of YAF has been done in part under the auspices of the Aix-Marseille I University in 1998 and 1999. YAF acknowledges also the support from the Russian Foundation for Basic Research (grant 98–02–16734).

References

Aggarwal K.M., Berrington K.A., Burke P.G., et al., 1991, J. Phys. B.: At. Mol. Opt. Phys. 24, 1385

Callaway J., 1994, Atomic Data and Nuclear Data Tables, 57, 9

Callaway J., Unnikrishan K., 1993, Phys. Rev. A 48, 4292

Fadeyev Yu.A., Gillet D., 1998, A&A 333, 687 (Paper I)

Feautrier P., 1964, C. R. Acad. Sci. Paris, 258, 3189

Gillet D., 1999, Rarefied Gas Dynamics, 21st International Symposium, Eds. Brun R., et al., Marseille 26-31 July 1998, Vol. II, 517

Gillet D., Lafon J.-P.J., 1990, A&A 235, 255

Kurucz R., 1970, SAO Special Report, No 309

Kuznetsov N.M., Raizer Yu. P., 1965, Zh. Priklad. Mekh. Tekh. Fiz. 4, 6

Marshak R.E., 1958, Phys. Fluids 1, 24

Mihalas D., 1967, ApJ 149, 169

Mihalas D., 1978, Stellar Atmospheres, 2nd Ed., Freeman, San Francisco

Mihalas D., Mihalas B.W., 1984, Foundations of Radiation Hydrodynamics, Oxford University Press, Oxford

Murty S.S.R., 1971, J. Quant. Spectrosc. Radiat. Transfer, 11, 1681

Narita S., 1973, Prog. Theor. Phys., 49, 1911

Rybicki G.B., Hummer D.G., 1991, A&A 245, 171

Scholz T.T., Walters H.R.J., 1991, ApJ 380, 302

Spitzer L., Härm R., 1953, Phys. Rev. 89, 977

Zel'dovich, Ya.B., Raizer, Yu.P., 1966, Physics of Shock Waves and High–Temperature Hydrodynamic Phenomena, Academic Press, New York